Probabilistic Robustness Analysis of F-16 Controller Performance: An Optimal Transport Approach

Abhishek Halder, Kooktae Lee, and Raktim Bhattacharya

***Abstract*— This paper presents an optimal transport theoretic formulation to assess the controller robustness for F-16 aircraft. We compare the state regulation performance for a linear quadratic regulator (LQR) and gain scheduled LQR (gsLQR), applied to nonlinear longitudinal open-loop dynamics of F-16, under stochastic initial condition uncertainty. It is shown that both controllers have comparable immediate and asymptotic performance, but gsLQR achieves better transient performance than LQR. Algorithms based on Perron-Frobenius operator, are given for tractable computation. Numerical results from the proposed method, are in unison with Monte Carlo simulations.**

I. Introduction

In systems and control, probabilistic robustness [1]–[5] has emerged as an alternative paradigm to classical worst-case robustness. The main motivation behind this development is to overcome: (i) the computational complexity [6]–[8], and (ii) the inherent conservatism in controller synthesis and analysis [9], [10]. To assess the performance of these risk-adjusted controllers, ideas such as robustness degradation function [2], [11], [12] have been proposed in the literature. However, numerical implementation of these performance assessment techniques mostly rely on Monte Carlo like realization-based algorithms, leading to high computational cost for implementing them to nonlinear systems.

This is a serious bottleneck in applications like flight control software certification [13], where the closed loop dynamics is nonlinear, and linear robustness analysis supported with Monte Carlo, remains the state-of-the art. Lack of nonlinear robustness analysis tools, coupled with the increasing complexity of flight control algorithms, have caused loss of several F/A-18 aircrafts due to nonlinear "falling leaf mode" [14], undetectable [15] by linear robustness analysis algorithms. On the other hand, accuracy of sum-of-squares optimization-based *deterministic* nonlinear robustness analysis [13], [14] depends on the quality of semi-algebraic approximation, and is still computationally expensive for large-scale nonlinear systems. Thus, there is a need for controller robustness verification methods, that does not make any structural assumption on nonlinearity, and allows scalable computation while accommodating stochastic uncertainty.

This paper presents computationally efficient algorithms for nonlinear robustness verification of controllers, in the presence of stochastic initial condition uncertainties. We consider the longitudinal dynamics of F-16, with linear quadratic regulator and gain-scheduled linear quadratic regulator. Perron-Frobenius operator based methods are used to propagate the uncertainties through closed-loop nonlinearities. Wasserstein distance of the instantaneous state ensemble from trim, is introduced as a measure of controller robustness. The proposed formulation departs from the existing literature in that both computation and analysis are done in nonparametric distributional sense. We argue this to be the main source of computational leverage since the Perron-Frobenius operator is linear, even though the underlying state dynamics is nonlinear. Moreover, we demonstrate that the distributional robustness assessment of the controllers' performance, lead to further simplification of Wasserstein computation. The inferences drawn from Wasserstein-based analysis are shown to be consistent with Monte Carlo predictions.

Rest of this paper is structured as follows. Section II describes the nonlinear open loop longitudinal dynamics for F-16 aircraft. The LQR and gsLQR controller synthesis are discussed in Section III. Section IV provides the uncertainty propagation techniques required for the controller verification step, detailed in Section V. Additional statistical analysis are performed in Section IV to provide qualitative insights about the controllers' performance, which are then verified by the quantitative transport theoretic results of Section V. Section VI concludes the paper.

Notation: Most notations are standard. Symbols x and u denote the state and control vectors. The state variables are pitch attitude θ (deg), total velocity V (ft/s), angle-of-attack α (deg), and pitch rate q (deg/s). The control variables T and δ_e denote thrust (lb) and elevator input (deg), respectively. The symbol $\mathrm{diag}(\cdot)$ denotes the diagonal matrix of appropriate dimensions, $\mathrm{supp}\,(\cdot)$ denotes support of a function, and $\mathcal{U}\,(\cdot)$ represents the uniform distribution.

II. F-16 Flight Dynamics

A. Longitudinal Equations of Motion

The longitudinal equations of motion for F-16 considered here, follows the model given in [16]–[18], with the exception that we restrict the maneuver to a constant altitude ($h = 10,000$ ft) flight. Further, the north position state equation is dropped since no other longitudinal states depend on it. This results a reduced *four state, two input model* with

Abhishek Halder, Kooktae Lee, and Raktim Bhattacharya are with the Department of Aerospace Engineering, Texas A&M University, College Station, TX 77843-3141, USA, {ahalder,animodor,raktim}@tamu.edu.This research was supported by NSF award #1016299 with Dr. Helen Gill as the Program Manager.

TABLE I

PARAMETERS IN EQN. (1)

Description of parameters	Values with dimensions
Mass of the aircraft	$m = 636.94$ slugs
Acceleration due to gravity	$g = 32.17$ ft/s^2
Wing planform area	$S = 300$ ft^2
Mean aerodynamic chord	$\bar{c} = 11.32$ ft
Reference x-position of c.g.	$x_{\text{cg}}^{\text{ref}} = 0.35\,\bar{c}$ ft
True x-position of c.g.	$x_{\text{cg}} = 0.30\,\bar{c}$ ft
Pitch moment-of-inertia	$J_{yy} = 55,814$ slug-ft^2
Nominal atmospheric density	$\rho_0 = 2.377 \times 10^{-3}$ slugs/ft^3

$x = (\theta, V, \alpha, q)^\top$, $u = (T, \delta_e)^\top$, given by

$$\dot{\theta} = q, \tag{1a}$$

$$\dot{V} = \frac{1}{m}\cos\alpha\left[T - mg\sin\theta + \bar{q}S\left(C_X + \frac{\bar{c}}{2V}C_{X_q}q\right)\right] + \frac{1}{m}\sin\alpha\left[mg\cos\theta + \bar{q}S\left(C_Z + \frac{\bar{c}}{2V}C_{Z_q}q\right)\right], \tag{1b}$$

$$\dot{\alpha} = q - \frac{\sin\alpha}{mV}\left[T - mg\sin\theta + \bar{q}S\left(C_X + \frac{\bar{c}}{2V}C_{X_q}q\right)\right] + \frac{\cos\alpha}{mV}\left[mg\cos\theta + \bar{q}S\left(C_Z + \frac{\bar{c}}{2V}C_{Z_q}q\right)\right], \tag{1c}$$

$$\dot{q} = \frac{\bar{q}S\bar{c}}{J_{yy}}\left[C_m + \frac{\bar{c}}{2V}C_{m_q}q + \frac{(x_{\text{cg}}^{\text{ref}} - x_{\text{cg}})}{\bar{c}}\left(C_Z + \frac{\bar{c}}{2V}C_{Z_q}q\right)\right]. \tag{1d}$$

The parameters in eqn. (1) are listed in Table I. Furthermore, the dynamic pressure $\bar{q} = \frac{1}{2}\rho(h)\,V^2$, where the atmospheric density $\rho(h) = \rho_0\left(1 - 0.703 \times 10^{-5}h\right)^{4.14} = 1.8 \times 10^{-3}$ slugs/ft^3 remains fixed.

B. Aerodynamic Coefficients

The aerodynamic force and moment coefficients C_X, C_Z, and C_m are functions of α and δ_e, expressed as look-up table from wind tunnel test data [16]–[18]. Similarly, the stability derivatives C_{X_q}, C_{Z_q}, and C_{m_q} are table look-up functions of α. We refer the readers to above references for details.

III. F-16 Flight Control Laws

In this paper, we consider two controllers: *linear quadratic regulator* (LQR) and *gain-scheduled linear quadratic regulator* (gsLQR), as shown in Fig. 1 and 2, respectively. Both controllers minimize the infinite-horizon cost functional

$$\mathcal{J} = \int_0^\infty \left(x^\top Q\,x + u^\top R\,u\right)\,dt, \tag{2}$$

with $Q = \text{diag}\left(100, 0.25, 100, 10^{-4}\right)$, and $R = \text{diag}\left(10^{-6}, 625\right)$. Further, the control saturation shown in the block diagrams, is modeled as

$$1000\,\text{lb} \leqslant T \leqslant 28,000\,\text{lb}, \quad -25^\circ \leqslant \delta_e \leqslant +25^\circ. \tag{3}$$

A. LQR Synthesis

The nonlinear open loop plant model was linearized about $x_{\text{trim}}, u_{\text{trim}}$, using simulink `linmod` command. The trim conditions were computed via the nonlinear optimization package SNOPT [19], and are given by $x_{\text{trim}} = \left(2.8190\,\text{deg}, 407.8942\,\text{ft/s}, 6.1650\,\text{deg}, 6.8463 \times 10^{-4}\,\text{deg/s}\right)^\top$, $u_{\text{trim}} = \left(1000\,\text{lb}, -2.9737\,\text{deg}\right)^\top$. The LQR gain K was computed for this linearized model.

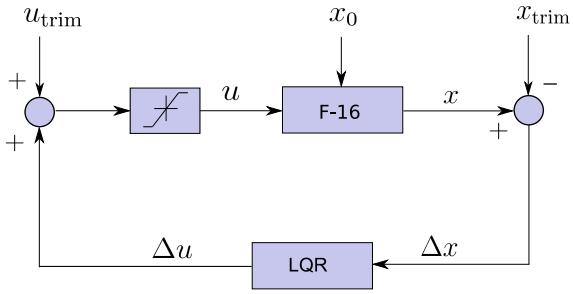

Fig. 1. Block diagram of LQR closed-loop system.

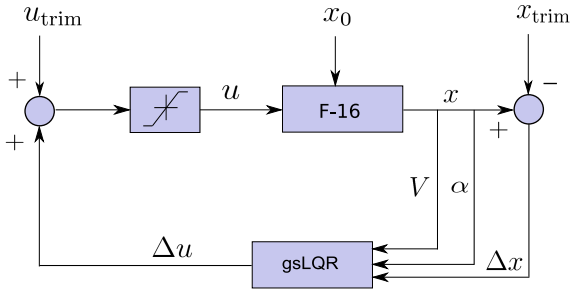

Fig. 2. Block diagram of gsLQR closed-loop system.

B. Gain-scheduled LQR Synthesis

As shown in Fig. 2, V and α are taken as the scheduling states. We generate 100 grid points in the box

$$100\,\text{ft/s} \leqslant V \leqslant 1000\,\text{ft/s}, \quad -10^\circ \leqslant \alpha \leqslant +45^\circ, \tag{4}$$

and compute trim conditions $\{x_{\text{trim}}^j, u_{\text{trim}}^j\}_{j=1}^{100}$, using SNOPT, for each of these grid points. Next, we synthesize a sequence of LQR gains $\{K_j\}_{j=1}^{100}$, corresponding to the linearized dynamics about each trim.

IV. Closed-loop Uncertainty Propagation

A. Perron-Frobenius Operator

To test the robustness of controller performance, we allow the initial condition to be a stochastic perturbation from x_{trim}, i.e. $x_0 = x_{\text{trim}} + x_{\text{pert}}$, where x_{pert} is a random vector from $\mathcal{U}\left(\left[\theta_{\text{pert}}^{\min}, \theta_{\text{pert}}^{\max}\right] \times \left[V_{\text{pert}}^{\min}, V_{\text{pert}}^{\max}\right] \times \left[\alpha_{\text{pert}}^{\min}, \alpha_{\text{pert}}^{\max}\right] \times \left[q_{\text{pert}}^{\min}, q_{\text{pert}}^{\max}\right]\right)$, where the perturbation range for each state, is listed in Table II.

Given a joint probability density function (PDF) φ_0 supported over x_0, we next compute the evolution of joint PDF $\varphi(x(t), t)$ subject to both LQR and gsLQR closed-loop dynamics. The *Perron-Frobenius (PF) operator* [20] framework allows us to do this computation *in exact arithmetic*, as described below.

TABLE II

ADMISSIBLE STATE PERTURBATION LIMITS

x_{pert}	Interval
$\theta_{\text{pert}} \in \left[\theta_{\text{pert}}^{\min}, \theta_{\text{pert}}^{\max}\right]$	$[-35^\circ, +35^\circ]$
$V_{\text{pert}} \in \left[V_{\text{pert}}^{\min}, V_{\text{pert}}^{\max}\right]$	$[-65$ ft/s, $+65$ ft/s$]$
$\alpha_{\text{pert}} \in \left[\alpha_{\text{pert}}^{\min}, \alpha_{\text{pert}}^{\max}\right]$	$[-20^\circ, +50^\circ]$
$q_{\text{pert}} \in \left[q_{\text{pert}}^{\min}, q_{\text{pert}}^{\max}\right]$	$[-70$ deg/s, $+70$ deg/s$]$

TABLE III

COMPARISON OF JOINT PDF COMPUTATION OVER $\mathbb{R}^d$: MC VS. PF

Attributes	MC simulation	PF via MOC
Concurrency	Offline post-processing	Online
Accuracy	Histogram approximation	Exact arithmetic
Spatial discretization	Grid based	Meshless
ODEs per sample	d	$d+1$

1) Liouville PDE formulation: The transport equation associated with the PF operator, governing the spatio-temporal evolution of probability mass over the state space, is given by the stochastic Liouville eqn.

$$\frac{\partial \varphi}{\partial t} = -\sum_{i=1}^{4} \frac{\partial}{\partial x_i} \left(\varphi \, f_{\text{cl}}\right), \qquad x\left(t\right) \in \mathbb{R}^4, \tag{5}$$

where $f_{\text{cl}}\left(x\left(t\right), t\right)$ denotes the closed-loop vector field. Since (5) is a first-order PDE, it allows method-of-characteristics (MOC) formulation, which we describe next.

2) Characteristic ODE computation: It can be shown [21] that the characteristic curves for (5), are the trajectories of the closed-loop ODE $\dot{x} = f_{\text{cl}}\left(x\left(t\right), t\right)$. If the nonlinear vector field f_{cl} is Lipschitz, then the trajectories are unique, and hence the characteristic curves are non-intersecting. Thus, instead of solving the PDE boundary value problem (5), we can solve the following initial value problem [21], [22]:

$$\dot{\varphi} = -\left(\nabla \cdot f_{\text{cl}}\right) \varphi, \qquad \varphi\left(x_0, 0\right) = \varphi_0, \tag{6}$$

along the trajectories $x\left(t\right)$. Notice that solving (6) along one trajectory, is independent of the other, and hence the formulation is a natural fit for parallel implementation. This computation differs from Monte Carlo (MC) as shown in Table III.

Notice that the divergence computation in (6) can be done analytically offline for our case of LQR and gsLQR closed-loop systems, provided we obtain function approximations for aerodynamic coefficients. However, even with analytical open-loop dynamics, this divergence computation does not scale for controllers (e.g. RHC) which numerically realize state-feedback. For these reasons, we implement an alternative online computation of divergence in this paper. Using `linmod`, we linearize the *closed-loop systems* about each characteristics, and obtain the instantaneous divergence as the trace of the time-varying Jacobian matrix.

B. Numerical Results

1) Simulation set up: We generate pseudo-random Halton sequence [23] in $\left[\theta_{\text{pert}}^{\min}, \theta_{\text{pert}}^{\max}\right] \times \left[V_{\text{pert}}^{\min}, V_{\text{pert}}^{\max}\right] \times \left[\alpha_{\text{pert}}^{\min}, \alpha_{\text{pert}}^{\max}\right] \times \left[q_{\text{pert}}^{\min}, q_{\text{pert}}^{\max}\right]$, to sample the uniform distribution φ_{pert}, and hence φ_0 supported on the four dimensional state space. With 2000 Halton samples for φ_0, we propagate joint state PDFs for both LQR and gsLQR closed-loop dynamics via MOC ODE (6), from $t = 0$ to 20 seconds, using fourth-order Runge-Kutta integrator with fixed step-size $\Delta t = 0.01$ s.

We observed that the `linmod` computation for evaluating time-varying divergence along each trajectory, takes the most of computational time. To take advantage of the fact that computation along characteristics are independent of each other, all simulations were performed using 12 cores with NVIDIA® Tesla GPUs in MATLAB® environment. It was noticed that with LQR closed-loop dynamics, the computational time for single sample from $t = 0$ to 20 s, is approx. 90 seconds. With sequential `for`-loops over 2000 samples, this scales to 50 hours of runtime. The same for gsLQR scales to 72 hours of runtime. In parallel implementation on Tesla, MATLAB® `parfor`-loops were used to reduce these runtimes to 4.5 hours (for LQR) and 6 hours (for gsLQR), respectively.

2) Results: Fig. 3 shows the evolution of univariate *marginal error PDFs*. All marginal computations were performed using algorithms previously developed by the authors [21]. Since φ_0 and its marginals were uniform, Fig. 3(a) shows similar trend for small t, and there seems no visible difference between LQR and gsLQR performance. As t increases, both LQR and gsLQR error PDFs shrink about zero. Clearly, by $t = 20$ s (Fig. 3(d)), both LQR and gsLQR controllers make the respective state marginals $\varphi^j\left(t\right)$, $j = 1, \ldots, 4$, converge to the Dirac distribution at x_{trim}^j, and hence individual error marginals become unit impulses at their respective zeros. Thus, Fig. 3 *qualitatively* show that both LQR and gsLQR exhibit comparable *immediate* and *asymptotic* performance, as far as robustness against initial condition uncertainty is concerned. However, there are some visible mismatches in Fig. 3(b) and 3(c), that suggests a careful quantitative investigation of the transient performance (Section V).

We can verify the insights obtained from Fig. 3 against the MC simulations (Fig. 4). Interestingly, Fig. 4(a) shows that LQR fails to stabilize some initial conditions to x_{trim}, while gsLQR is robust for all initial perturbations (Fig. 4(b)). However, Fig. 5 shows that the failure of LQR controller is a low-probability event. Hence in risk-aware perspective, LQR is asymptotically stabilizing in distributional sense, as predicted by Fig. 3(d). In other words, gsLQR has better asymptotic performance than LQR, but this improvement is probabilistically not significant. Furthermore, the most probable state errors for LQR and gsLQR (*top row* in Fig. 6) match well, but the corresponding least probable state errors (*bottom row* in Fig. 6) have transient mismatch. The latter also shows that the low-probability divergent LQR trajectories are *not least likely*.

V. OPTIMAL TRANSPORT TO TRIM

A. Wasserstein Metric

To provide a quantitative comparison for LQR and gsLQR controllers' performance, we need a notion of "distance" between the respective time-varying state PDFs and the desired state PDF. Since the controllers strive to bring the state trajectory ensemble to x_{trim}, hence we take $\varphi^*\left(x_{\text{trim}}\right)$, a Dirac delta distribution at x_{trim}, as our desired joint PDF. The notion of distance must compare the concentration of trajectories in the state space and for meaningful inference, should define a metric. Next, we describe Wasserstein metric,

that meets these axiomatic requirements [24] of "distance" on the manifold of PDFs.

1) Definition: Consider the metric space (M, ℓ_2) and take $x, \widetilde{x} \in M$. Let $\mathcal{P}_2(M)$ denote the collection of all probability measures μ supported on M, which have finite 2^{nd} moment. Then the L_2 Wasserstein distance of order 2, denoted as ${}_2W_2$, between two probability measures $\varsigma_1, \varsigma_2 \in \mathcal{P}_2(M)$, is defined as

$$ {}_2W_2(\varsigma_1, \varsigma_2) := \left(\inf_{\mu \in \mathcal{M}(\varsigma_1, \varsigma_2)} \int_{M \times M} \| x - \widetilde{x} \|_{\ell_2}^2 \; d\mu(x, \widetilde{x}) \right)^{\frac{1}{2}} $$

where $\mathcal{M}(\varsigma_1, \varsigma_2)$ is the set of all measures supported on the product space $M \times M$, with first marginal ς_1 and second marginal ς_2.

Intuitively, Wasserstein distance equals the *least amount of work* needed to convert one distributional shape to the other, and can be interpreted as the cost for Monge-Kantorovich optimal transportation plan [25]. The particular choice of L_2 norm with order 2 is motivated in [26]. For notational ease, we henceforth denote ${}_2W_2$ as W. One can prove (p. 208, [25]) that W defines a metric on the manifold of PDFs.

2) Computation of W: In general, one needs to compute W from its definition, which requires solving a *linear program* (LP) [24] in mn variables, subject to $(m + n + mn)$ constraints, with m and n being the cardinality of the respective scattered data representation of the PDFs under comparison. As shown in [26], the main source of computational burden stems from *storage complexity*. It is easy to verify that the *sparse constraint matrix representation* requires $(6mn + (m+n)d + m + n)$ amount of storage, while the same for *non-sparse representation* is $(m+n)(mn + d + 1)$, where d is the dimension of the support for each PDF. Notice that d enters linearly through ℓ_2 norm computation, but the storage complexity grows *polynomially* with m and n. We observed that with sparse LP solver MOSEK [27], on a standard computer with 4 GB memory, one can go up to $m = n = 3000$ samples. On the other hand, increasing the number of samples, increases the accuracy [26] of finite-sample W computation. This leads to numerical accuracy versus storage capacity trade off.

3) Reduction of storage complexity: For our purpose of computing $W(\varphi(x(t), t), \varphi^*(x_{\text{trim}}))$, the storage complexity can be reduced by leveraging the fact that $\varphi^*(x_{\text{trim}})$ is a stationary Dirac distribution. Hence, it suffices to represent the joint probability mass function (PMF) of $\varphi^*(x_{\text{trim}})$ as a single sample located at x_{trim} with PMF value unity. This trivializes the optimal transport problem, since

$$ \begin{aligned} W(t) &\triangleq W(\varphi(x(t), t), \varphi^*(x_{\text{trim}})) \\ &= \sqrt{\sum_{i=1}^{n} \| x_i(t) - x_{\text{trim}} \|_2^2 \; \gamma_i}, \end{aligned} \tag{7} $$

where $\gamma_i \geqslant 0$ denotes the joint PMF value at sample $x_i(t)$, $i = 1, \ldots, n$. Consequently, the storage complexity reduces to $(nd + n + d)$, which is *linear* in number of samples.

B. Numerical Results

We compute the time-evolution of the two Wasserstein distances

$$ \begin{aligned} W_{\text{LQR}}(t) &\triangleq W(\varphi_{\text{LQR}}(x(t), t), \varphi^*(x_{\text{trim}})), \\ W_{\text{gsLQR}}(t) &\triangleq W(\varphi_{\text{gsLQR}}(x(t), t), \varphi^*(x_{\text{trim}})). \end{aligned} $$

The overall simulation framework is depicted in Fig. 7.

Fig. 8 indeed confirms the qualitative trends, mentioned in Section IV.B.2, that LQR and gsLQR exhibit comparable immediate and asymptotic performance. Furthermore, Fig. 8 shows that for $t = 3{-}8$ seconds, W_{LQR} is significantly higher than W_{gsLQR}, meaning the gsLQR joint PDF $\varphi_{\text{gsLQR}}(x(t), t)$ is closer to $\varphi^*(x_{\text{trim}})$, compared to the LQR joint PDF $\varphi_{\text{LQR}}(x(t), t)$. This corroborates well with the mismatch observed in Fig. 3(c). As time progresses, both W_{LQR} and W_{gsLQR} converge to zero, meaning the convergence of both LQR and gsLQR joint PDFs to the Dirac distribution at x_{trim}.

At this point, we emphasize that the Wasserstein closeness results are necessary and sufficient since W is a metric, and it computes the distance between joints. In other words, Fig. 3 only provides sufficiency results since convergence of joints imply convergence of marginals, but the converse is not true. Further, since $W_{\text{LQR}}(t) \to 0$ for large t, we can affirmatively say that the divergent LQR trajectories are indeed of low-probability. Otherwise, $W_{\text{LQR}}(t)$ would show a steady-state error. Thus, the Wasserstein distance is shown to be an effective way of comparing the performance of controllers.

VI. Conclusions

In this paper, we compare the performance of two controllers, viz. LQR and gsLQR, for F-16 longitudinal dynamics with stochastic initial condition uncertainty. We propose a set of tools for distributional robustness analysis of these two controllers, based on Perron-Frobenius operator and Monge-Kantorovich optimal transport. It is shown that the new framework allows scalable computation for large nonlinear systems, without making any *a-priori* structural assumption about the nonlinearity or uncertainty. We show that both LQR and gsLQR have comparable immediate and asymptotic performance, but the transient performance of gsLQR is found to be more robust than that of the LQR. These inferences are substantiated with marginal statistics and Monte Carlo simulation.

References

[1] B.R. Barmish, "Probabilistic Robustness: A New Line of Research", *UKACC International Conference on (Conf. Publ. No. 427) Control'96*, Vol. 1, pp. 181–181, 1996.

[2] G.C. Calafiore, and F. Dabbene, and R. Tempo, "Randomized Algorithms for Probabilistic Robustness with Real and Complex Structured Uncertainty", *IEEE Transactions on Automatic Control*, Vol. 45, No. 12, pp. 2218–2235, 2000.

[3] B.T. Polyak, and R. Tempo, "Probabilistic Robust Design with Linear Quadratic Regulators", *Systems & Control Letters*, Vol. 43, No. 5, pp. 343–353, 2001.

[4] Q. Wang, and R.F. Stengel, "Robust Control of Nonlinear Systems with Parametric Uncertainty", *Automatica*, Vol. 38, No. 9, pp. 1591–1599, 2002.

[5] X. Chen, J.L. Aravena, and K. Zhou, "Risk Analysis in Robust Control–Making the Case for Probabilistic Robust Control", *Proceedings of the 2005 American Control Conference*, pp. 1533–1538, 2005.

[6] P. Khargonekar, and A. Tikku, "Randomized Algorithms for Robust Control Analysis and Synthesis Have Polynomial Complexity", *Proceedings of the 35th IEEE Conference on Decision and Control*, Vol. 3, pp. 3470–3475, 1996.

[7] R. Tempo, E.W. Bai, and F. Dabbene, "Probabilistic Robustness Analysis: Explicit Bounds for the Minimum Number of Samples", *Proceedings of the 35th IEEE Conference on Decision and Control*, Vol. 3, pp. 3470–3475, 1996.

[8] M. Vidyasagar, and V.D. Blondel, "Probabilistic Solutions to Some NP-hard Matrix Problems", *Automatica*, Vol. 37, No. 9, pp. 1397–1405, 2001.

[9] C.M. Lagoa, P.S. Shcherbakov, and B.R. Barmish, "Probabilistic Enhancement of Classical Robustness Margins: The Unirectangularity Concept", *Proceedings of the 36th IEEE Conference on Decision and Control*, Vol. 5, pp. 4874–4879, 1997.

[10] C.M. Lagoa, "Probabilistic Enhancement of Classical Robustness Margins: A Class of Nonsymmetric Distributions", *IEEE Transactions on Automatic Control*, Vol. 48, No. 11, pp. 1990–1994, 2003.

[11] B.R. Barmish, C.M. Lagoa, and R. Tempo, "Radially Truncated Uniform Distributions for Probabilistic Robustness of Control Systems", *Proceedings of the 1997 American Control Conference*, Vol. 1, pp. 853–857, 1997.

[12] X. Chen, K. Zhou, and J.L. Aravena, "Fast Construction of Robustness Degradation Function", *Proceedings of the 41st IEEE Conference on Decision and Control*, Vol. 2, pp. 2242–2247, 2002.

[13] A. Chakraborty, P. Seiler, and G.J. Balas, "Nonlinear Region of Attraction Analysis for Flight Control Verification and Validation", *Control Engineering Practice*, Vol. 19, No. 4, pp. 335–345, 2011.

[14] P. Seiler, and G.J. Balas, and A. Packard, "Assessment of Aircraft Flight Controllers using Nonlinear Robustness Analysis Techniques", *Optimization Based Clearance of Flight Control Laws*, Lecture Notes in Control and Information Sciences, Vol. 416, Springer, pp. 369–397, 2012.

[15] A. Chakraborty, P. Seiler, and G.J. Balas, "Susceptibility of F/A-18 Flight Controllers to the Falling-Leaf Mode: Linear Analysis", *Journal of Guidance, Control, and Dynamics*, Vol. 34, No. 1, pp. 57–72, 2011.

[16] L.T. Nguyen, M.E. Ogburn, W.P. Gilbert, K.S. Kibler, P.W. Brown, and P.L. Deal, "Simulator Study of Stall/Post-stall Characteristics of A Fighter Airplane with Relaxed Longitudinal Static Stability", *NASA TP 1538*, December, 1979.

[17] B.L. Stevens, and F.L. Lewis, *Aircraft Control and Simulation*, John Wiley, 1992.

[18] R. Bhattacharya, G.J. Balas, A. Kaya, and A. Packard, "Nonlinear Receding Horizon Control of F-16 Aircraft", *Proceedings of the 2001 American Control Conference*, Vol. 1, pp. 518–522, 2001.

[19] P.E. Gill, W. Murray, and M.A. Saunders, "User's Guide for SNOPT Version 7: Software for Large-Scale Nonlinear Programming", *Technical Report*, Available at `http://www.ccom.ucsd.edu/~peg/papers/sndoc7.pdf`.

[20] A. Lasota, and M.C. Mackey, *Chaos, Fractals, and Noise: Stochastic Aspects of Dynamics*, Springer, Vol. 97, 1994.

[21] A. Halder, and R. Bhattacharya, "Dispersion Analysis in Hypersonic Flight During Planetary Entry Using Stochastic Liouville Equation", *Journal of Guidance Control and Dynamics*, Vol. 34, No. 2, pp. 459–474, 2011.

[22] A. Halder, and R. Bhattacharya, "Beyond Monte Carlo: A Computational Framework for Uncertainty Propagation in Planetary Entry, Descent and Landing", *AIAA Guidance, Navigation and Control Conference*, Toronto, 2010.

[23] H. Niederreiter, *Random Number Generation and Quasi-Monte Carlo Methods*, CBMS-NSF Regional Conference Series in Applied Mathematics, SIAM, 1992.

[24] A. Halder, and R. Bhattacharya, "Model Validation: A Probabilistic Formulation", *IEEE Conference on Decision and Control*, Orlando, Florida, 2011.

[25] C. Villani, *Topics in Optimal Transportation*. Graduate Studies in Mathematics, First ed., American Mathematical Society; 2003.

[26] A. Halder, and R. Bhattacharya, "Further Results on Probabilistic Model Validation in Wasserstein Metric", *IEEE Conference on Decision and Control*, Maui, 2012.

[27] A.S. Mosek, "The MOSEK Optimization Software", Available at `http://www.mosek.com`, 2010.

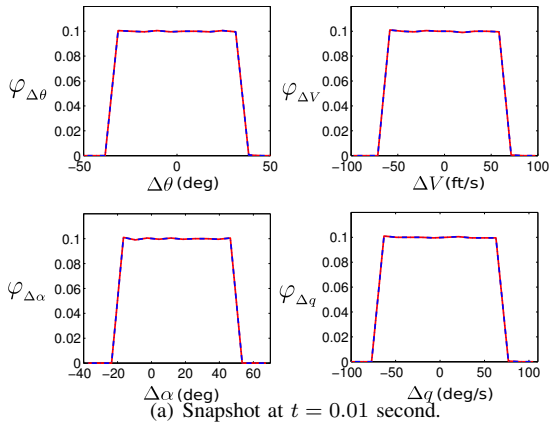

(a) Snapshot at $t = 0.01$ second.

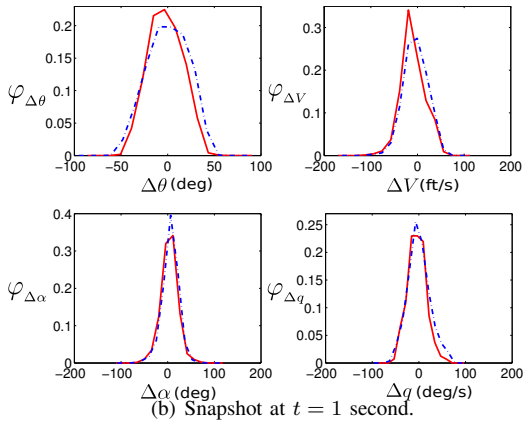

(b) Snapshot at $t = 1$ second.

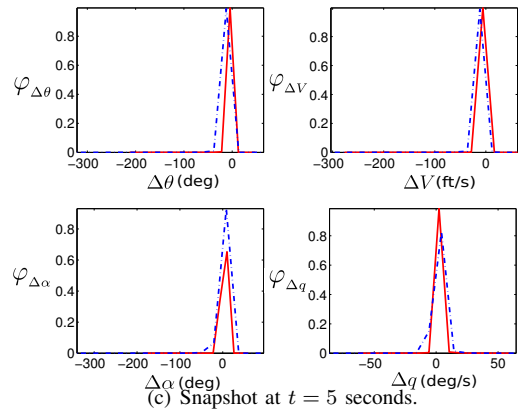

(c) Snapshot at $t = 5$ seconds.

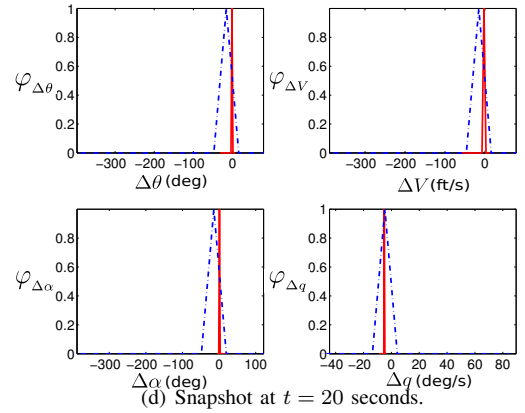

(d) Snapshot at $t = 20$ seconds.

Fig. 3. Snapshots of univariate marginal error PDFs for each state, with LQR *(blue, dashed)* and gsLQR *(red, solid)* closed loop dynamics.

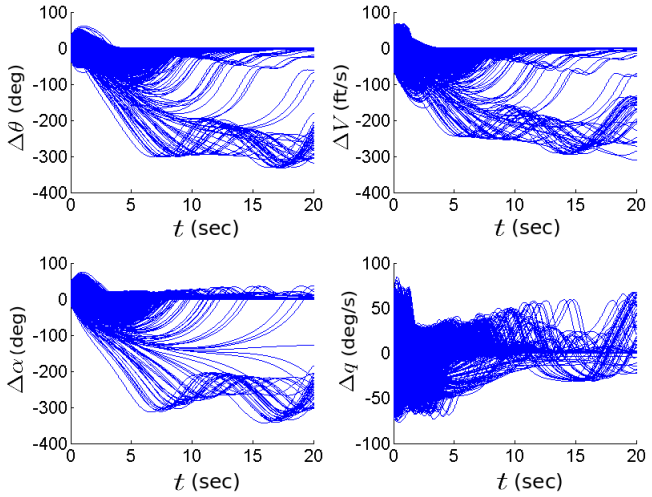

(a) State error vs. time for LQR controller

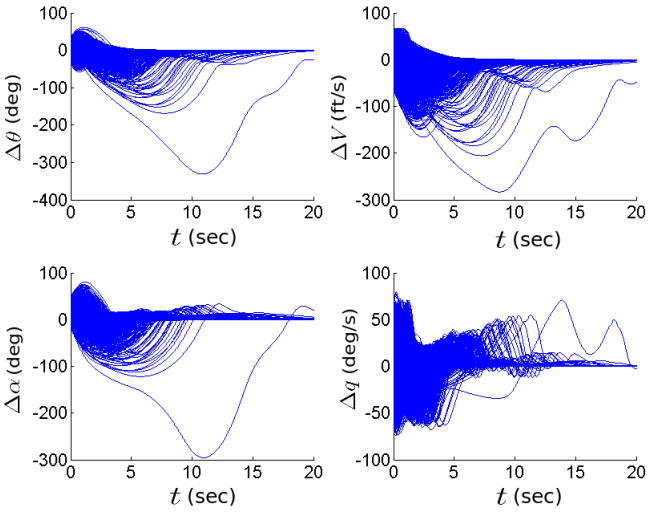

(b) State error vs. time for gsLQR controller

Fig. 4. MC state error ($\Delta x^j(t) \triangleq x^j(t) - x^j_{\text{trim}}$, $j = 1, \ldots, 4$) trajectories for LQR and gsLQR closed-loop dynamics.

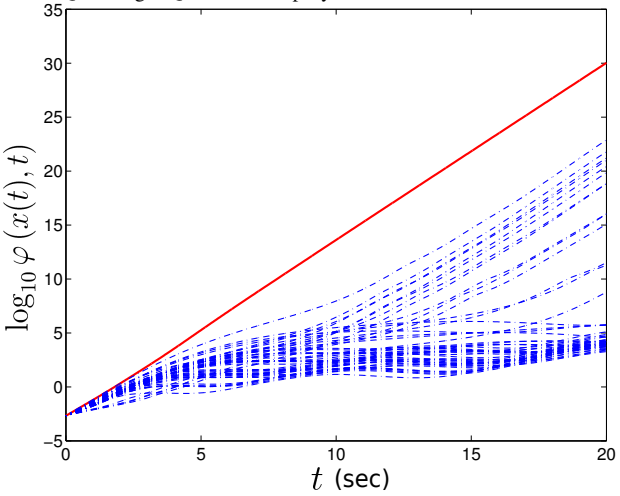

Fig. 5. Time evolution of *maximum value* of joint PDF $\varphi_{\text{LQR}}(x(t), t)$ (*red solid*) and $\varphi_{\text{LQR}}(x(t), t)$ *along the diverging trajectories* (*blue dashed*), as seen in Fig. 4(a). Since $\varphi_{\text{LQR}}(x(t), t)$ along a trajectory increases exponentially with time, the plots are linear in *log-linear* scale.

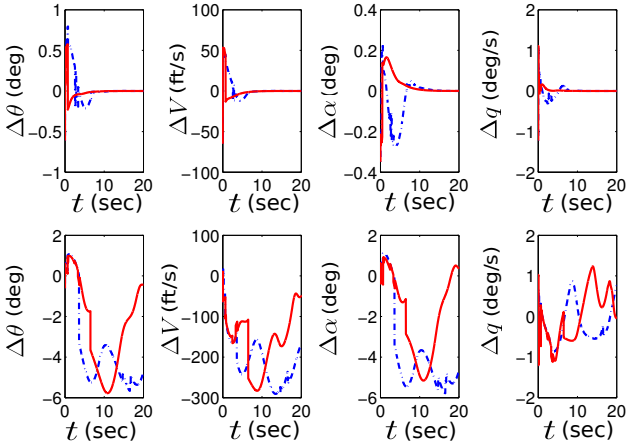

Fig. 6. Time evolution of the most likely (*top row*) and least likely (*bottom row*) state errors for LQR (*blue dashed*) and gsLQR (*red solid*) closed-loop dynamics.

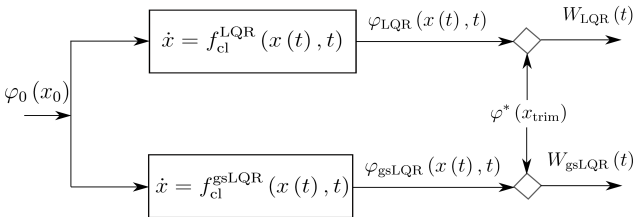

Fig. 7. Schematic of probabilistic robustness comparison for controllers based on Wasserstein metric. The "diamond" denotes the Wasserstein computation by solving the Monge-Kantorovich optimal transport. The internal details of LQR and gsLQR closed-loop dynamics blocks are as in Fig. 1 and 2, respectively.

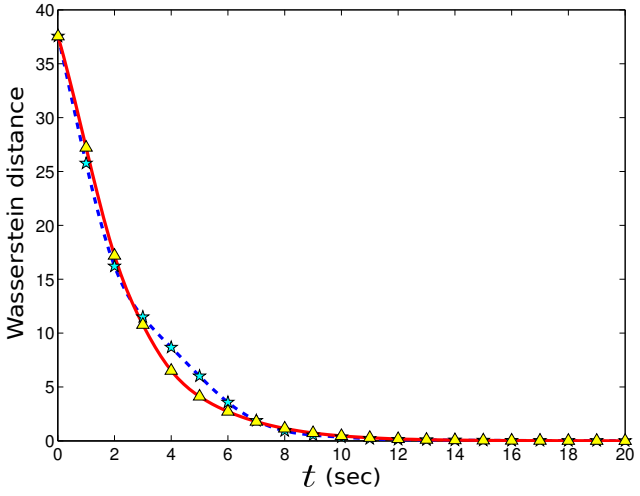

Fig. 8. Comparison of time histories of $W(\varphi_{\text{LQR}}(t), \varphi^*)$ *(blue dashed, star)* and $W(\varphi_{\text{gsLQR}}(t), \varphi^*)$ *(red solid, triangle).*